Magnetoresistance and Microstructure of Magnetite Nanocrystals Dispersed in Indium–Tin Oxide Thin Films

Magnetoresistance and microstructure of magnetite nanocrystals dispersed indium tin oxide thin films

Koichi Okada, Shigemi Kohiki,* Masanori Mitome,[†] Hidekazu Tanaka,[‡] Masao Arai,[†] Masaki Mito,[§] and Hiroyuki Deguchi[§]

Department of Materials Science and [§]*Department of Basic Science, Kyushu Institute of Technology, 1-1 Sensui, Tobata, Kitakyushu 804-8550, Japan*

[†]*National Institute for Materials Science, 1-1 Namiki, Tsukuba, Ibaraki 305-0044, Japan*

[‡]*Institute of Scientific and Industrial Research, Osaka University, 8-1 Mihogaoka, Ibaraki, Osaka 567-0047, Japan*

ABSTRACT Epitaxial indium tin oxide (ITO) thin films were fabricated on yttria-stabilized zirconia (YSZ) substrate by pulsed-laser deposition using magnetite (Fe_3O_4) nanoparticles dispersed ITO powders as a target. Magnetoresistance of the film at the field of 1 T was 39 % at 45 K, and it stayed at 3 % above 225 K. The film demonstrated cooling hysteresis in temperature dependence of *dc* magnetization. Transmission electron microscopy revealed that phase-separated Fe_3O_4 nanocrystals with width of ≈40-150 nm and height of ≈10-25 nm precipitated and grew epitaxially on the substrate in the film. Both the Fe_3O_4 (111) and ITO (001) planes were parallel to the YSZ (001) plane. The Fe_3O_4 (11-2) and (1-10) planes were parallel to the ITO (100) and (010) planes,

respectively, and the planes connected smoothly at grain boundary. Contour map of the electron density for the Fe_3O_4 (111) plane by the first-principles electronic structure computation was similar to that for the ITO (001) plane. The [111] oriented Fe_3O_4 nanocrystals played a role of spin-aligner for charge carriers of the epitaxial ITO film.

KEYWORDS: magnetoresistance, microstructure, magnetite nanocrystals, indium tin oxide thin film, epitaxial growth, pulsed-laser deposition

INTRODUCTION

Intense research has been carried out on room temperature ferromagnetism (*RT-FM*) of transparent conducting oxides (TCO) doped with 3*d* transition metal elements to explore promising material realizing transparent spintronics devices (1-20). Substitution of cation sites by the doped atoms was believed to be indispensable for realizing *RT-FM* in TCO, while *RT-FM* in TCO caused by ferromagnetic metal-clusters of the doped elements has also been reported (2, 4, 19). Indium tin oxide (ITO) is the most widely used TCO in semiconductor and electronic device industry. *RT-FM* was manifested for ITO films doped with Mn (8), Cr (13), and Fe (18). Pulsed-laser deposited (PLD) thin films grown heteroepitaxially on yttria-stabilized zirconia (YSZ) substrate in oxygen partial pressures of $10^{-3} \sim 10^{-1}$ Pa exhibited *RT-FM* due to nanocrystals (NCs) of γ-Fe_2O_3 dispersed in ITO (18). The mismatch between the lattice constant of the *a* axis of In_2O_3 (1.0118 nm) and twice of that of YSZ (0.5139 nm) amounted to 1.6 %. *RT-FM* due to

phase-separated Fe_3O_4 nanoparticles dispersed in ITO was also reported for the powders heat-treated at 900 ^oC in flowing argon gas (20). It is well known that Fe_3O_4 has the fully spin-polarized half-metallic band structure with the Curie temperature of 858 K, and it is highly conducting at room temperature. ITO containing phase-separated Fe_3O_4 NCs is anticipated to exhibit *RT-FM* due to charge carriers with spins parallel to the minority spins of Fe_3O_4 when the Fe_3O_4 [111] axis of the NCs are in parallel with each other.

Here, we report magnetoresistance and transmission electron microscopy of epitaxial ITO films fabricated on YSZ substrate by using the Fe_3O_4 nanoparticles dispersed ITO powders as a PLD-target in oxygen partial pressures lower than 5×10^{-6} Pa. The ratio of electrical resistance measured with the field of H = 1 T to that measured without the field varied from 0.72 at 45 K to 0.97 above 225 K with rising the temperature. Transmission electron microscopy revealed that phase-separated Fe_3O_4 NCs with width of ≈40-150 nm and height of ≈10-25 nm precipitated and grew epitaxially on the substrate in the film. The Fe_3O_4 [111] axis of each NC was vertical to the film surface. Smooth connection in the electron density distribution between the Fe_3O_4 (111) and the ITO (001) planes was simulated by the first-principles electronic structure computation.

EXPERIMENT AND COMPUTATION

Pulsed-Laser Deposition. We synthesized the Fe_3O_4 nanoparticles dispersed ITO powders for preparation of the PLD-target. For synthesis of ITO powders, weighed powders of In_2O_3 and SnO_2 with the molar ratio of In : Sn = 1.95 : 0.05 were mixed in

grinding, and then heated at 1200 ^{o}C in flowing Ar gas. The ITO powders were soaked to an ethanol solution of $FeCl_3$, and then dried and heated at 900 ^{o}C in flowing Ar gas. The molar ratio of In : Fe = 2 : 0.15 was determined by energy-dispersive x-ray analysis. The Fe_3O_4 nanoparticles dispersed ITO powders demonstrated x-ray diffraction (XRD) peaks attributable to the *C*-rare earth type In_2O_3 cubic cell. No XRD peak from any Fe related compounds appeared, while temperature dependence of *dc* magnetization (*M*-*T* curve) showed cooling hysteresis and a cusp around 120 K (see *Supporting Information* Figure S1) which corresponds to the Verwey transition temperature (T_V) of Fe_3O_4 bulk (20). For the usage as a target of PLD, the Fe_3O_4 nanoparticles dispersed ITO powders were pelletized, and then sintered at 1500 ^{o}C for 1 h in flowing oxygen gas. Thin films were grown on the (001) surface of YSZ substrate at 600 ^{o}C in a pressure lower than 5×10^{-6} Pa by using the Fe_3O_4 nanoparticles dispersed ITO target. ArF excimer laser with the wavelength of 193 nm was focused onto the target. Repetition rate and energy density were 3 Hz and 1 Jcm^{-2}, respectively. The deposition rate was ≈0.01 nms^{-1}. XRD pattern of the films were measured with a Rigaku CN2013 diffractometer using Cu *K*α radiation.

Physical Properties, Microstructure and Chemical States. For electric and magnetic measurements, we used a Quantum Design superconducting quantum interference devise (SQUID) magnetometer (PPMS 5S). Platinum electrodes with thickness of a few 100 nm were made by sputtering on the films, and they were bonded by gold wires to the system. For *M*-*T* measurement, the sample was cooled from room temperature to 5 K in zero-field, then the field of *H* = 100 Oe was applied. We measured

zero-field cooled (*ZFC*) magnetization with rising temperature up to 300 K. After the measurement, the sample was cooled again to 5 K in the same field, then field cooled (*FC*) magnetization was measured with increasing temperature to 300 K. Diamagnetism of both the ITO film and the YSZ substrate were compensated by using a bit of lead metal. Microstructure of the films was examined by a JEOL JEM-3100FEF transmission electron microscope (TEM) operated at the electron acceleration voltage of 300 kV. The TEM has an in-column omega-type energy filter that is useful to remove inelastic scattering contribution from electron diffraction patterns, and to map elemental distributions from energy-filtered images with ~0.5 nm spatial resolution. The Fe-maps representing distribution of iron atoms were obtained from the Fe L_3 electron energy loss signal. Energy-dispersive x-ray spectrometer attached on the TEM was also used for elemental analysis. X-ray absorption near edge structure (XANES) measurement was carried out at the BL15 in the SAGA-Light Source, Japan. The Fe *K* edge spectrum was collected at room temperature with the energy resolution of 10^{-4} ~ 10^{-3} by the conversion electron yield method.

Computation. The first-principles computation was carried out to examine in detail connection in the electron density between the Fe_3O_4 (111) and In_2O_3 (002) planes. The calculations were performed using the WIEN2k code, which is based on the APW + lo method (21). We used the generalized-gradient approximation for the density functional theory. Muffin-tin radii were chosen as 1.93 a.u. for In, 1.83 a.u. for Fe and 1.62 a.u. for oxygen. The cutoff wave number *K* for basis functions was set to be $RK = 6.0$, where *R* is

the smallest muffin-tin radius of 1.62 a.u. The number of *k*-points in an irreducible Brillion zone was chosen as 100. With these parameters, sufficient numerical convergences were achieved.

RESULTS AND DISCUSSION

Epitaxial Growth and Magnetoresistance of the ITO Film. As shown by the inset of Fig. 1 upper panel, XRD pattern indicates that the ITO film grew epitaxially on the YSZ substrate. We observed intense (*h*00) reflections from In_2O_3 cubic cell along with those of YSZ cubic cell. Furthermore, no peak from Fe related phase appeared, as seen in the upper panel of Fig. 1. The lattice constant *a* of the ITO film estimated from the (006) reflection was 1.008 nm. It is well known that the ionic radius of Sn^{4+} ion is smaller than that of In^{3+} ion. The *a* value of the *C*-rare earth type cubic cell was deceased by the Sn^{4+} ion substitution for In^{3+} ion. The mismatch between the lattice constant of the *a* axis of the ITO film and twice of that of the YSZ substrate amounted to 1.9 %. As shown in the lower panel of Fig. 1, the high-resolution TEM (HRTEM) image reconfirmed epitaxial growth of the ITO film on the YSZ substrate. Parallelism between the ITO (002) plane and the YSZ (002) plane seen in the HRTEM image is consistent with that observed by XRD. The ITO (200) plane is parallel to the YSZ (200) plane. The epitaxial orientation relation between the film and the substrate can be expressed as ITO (001) // YSZ (001) and ITO [100] // YSZ [100].

Figure 2 shows temperature dependence of resistance measured with (R_H) and without

(R_0) the magnetic field. Both resistance curves showed smooth decrease with rising temperatures. No sudden change at T_V is similar to that reported for the [111] oriented Fe_3O_4 film (22). As shown by the inset of Fig. 2, the R_H/R_0 value increased from 0.72 to 0.97 with rise of the temperature from 45 to 225 K, and the value remained at constant above 225 K. The values at 75 and 165 K were 0.74 and 0.95, respectively. R_H/R_0 above 225 K is almost the same as that reported as 0.98 at 300 K for the Fe_3O_4 films (22). Magnetoresistance (MR) defined as $[100 \times (R_0 - R_H) / R_H]$ at 45, 75, 105, 165, and above 225 K amounted to 39, 35, 18, 5, and 3 %, respectively. We observed a significant rise in MR with lowering temperature below 165 K, which is similar to that reported (22) below ≈180 K. The ratio of MR at 75 K to that at 165 K for the film (≈7) was rather large than the one (≈3.3) reported (22). Such change in MR is intriguing in relation to the film structure with the Fe_3O_4 and ITO heterointerface or with the Fe_3O_4 antiphase grain boundary (22). As mentioned below, the sample includes Fe_3O_4 NCs with the [111] axis vertical to the film plane. Since the [111] axis is the easy magnetization axis of the cubic Fe_3O_4 crystal, the magnetocrystalline anisotropy of Fe_3O_4 crystal brings about the spontaneous magnetization vertical to the film plane. The magnetization oriented to upward and downward are possible and equivalent for each NC without external magnetic field. When we assume magnetic coupling over a large fraction of the NCs is antiferromagnetic, a high resistance for the spin polarized electrons is there between the adjacent NCs. By application of magnetic field, the antiferromagnetically coupled spins are forced to align along the external field, and then transfer of the spin polarized

electrons will be enhanced.

MR of the film varied rapidly from 75 to 165 K, however, we found no magnetic anomaly at the temperatures in the *M-T* curves, as shown in Fig. 2. The film exhibited divergence between *FC* and *ZFC* magnetization. Above 50 K, the *M-T* curves of the film correspond well to that reported for the Fe_3O_4 nanoparticles with diameter of 50 nm (23). A broad maximum centered around 300 K in the *ZFC* magnetization, corresponding to blocking of superparamagnetic moments, was also reported for the Fe_3O_4 nanoparticles with diameter of 50 nm (23). It is known for Fe_3O_4 that shrinkage in nanoparticle diameter and in film thickness lowers T_V (24). Such magnetic behavior suggests that the ITO film is a magnetically diluted system of phase-separated Fe_3O_4 NCs (25), while the MR of the ITO film indicates that the carriers are highly spin-polarized almost the same as the epitaxial Fe_3O_4 films (26).

Precipitation and Epitaxy of Fe_3O_4 Nanocrystals. By using TEM we observed phase-separated Fe_3O_4 NCs with width of ≈40-150 nm and height of ≈10-25 nm located at interface between the ITO film and the YSZ substrate. As shown in the upper left panel of Fig. 3, surface of the ITO film with thickness of ≈75 nm is smooth, and a NC with width and height of ≈40 and ≈10 nm, respectively, located at the film-substrate interface. The NC includes iron atoms, as shown by the lower left panel of Fig. 3. Width and height of the NC including iron atoms reached ≈150 nm and ≈25 nm, respectively, for a larger NC, as shown in the upper and lower right panels of Fig. 3. Interestingly, both the smaller and larger NCs positioned at the film-substrate interface. Precipitation

of metal-clusters of the doped elements in oxide has been reported rather frequently, such as metallic Co-clusters in TiO_2 thin films (19), though there has been no report on NCs of metal oxides epitaxially grown on substrate in TCO films.

NCs of inverse spinel type Fe_3O_4 grew epitaxially on the YSZ substrate, as shown in Fig. 4. Two kinds of orientation were observed for Fe_3O_4 NCs from electron diffraction analysis. One is a [1-10] incidence and the other is a [11-2] incidence. In both orientations the Fe_3O_4 (111) plane is always parallel to the YSZ (002) plane. One orientation can be reproduced by rotating the other orientation by 90 degrees. The YSZ (001) surface and ITO crystal have four-fold symmetry along the surface normal and thus the two orientations are equivalent each other. The Fe_3O_4 NCs can be rotated along the surface normal by each 90 degrees and four types of orientation are possible.

A cubic structure for iron oxide that is different from the inverse spinel type Fe_3O_4 (a = 0.8396 nm) is well known as γ-Fe_2O_3 (a = 0.8346 nm). Lattice constants for the structures are very close and it is difficult to distinguish one from the other. However, the space groups are different for each other. It is Fd-3m for Fe_3O_4 and $P4_132$ for γ-Fe_2O_3. {112} reflections are forbidden for Fm3m symmetry but they are allowed in $P4_332$ symmetry. The electron diffraction pattern demonstrated no {112} reflection marked as × in the middle left panel of Fig. 4, and thus it is clear that the NCs are Fe_3O_4 crystals.

We reconfirmed that the chemical state of the NC including Fe atoms in the ITO film is Fe_3O_4 by the XANES spectrum shown in Fig. 5. It is well known that in the XANES spectra of 3*d* transition metal oxides photoexcitation of a 1*s* electron into the 3*d*-4*p*

mixed states at the central atom and the 4*p* continuum states brings about the pre-edge and the main peaks, respectively. Furthermore, multiple scattering from neighboring atom shells forms the secondary peak appearing at >10 eV above the main peak. The pre-edge peak at 7113 eV, the main peak at 7130 eV and the secondary peak at 7145 eV in Fig. 5 agree well with those reported for Fe_3O_4 (27).

As it seen, the ITO film grew epitaxially even on the surface of Fe_3O_4 NC. The most interesting fact is that Fe atoms supplied from the PLD-target were excluded and segregated from the single crystalline ITO matrix, and formed truncated tetrahedron (Fig. 6) of Fe_3O_4 on the substrate (28). In this figure one example of the Fe_3O_4 orientations is shown. The Fe_3O_4 island can be rotated on the surface in each 90 degrees along the surface normal as mentioned before. Nucleation of three-dimensional islands is popular at the initial stage of thin film growth on a substrate having a different lattice constant. For releasing the strain energy due to the lattice mismatch, the three-dimensional island formation is effective even for films too thin to form dislocations (29). The mismatch between the lattice constant *a* of Fe_3O_4 and that of ITO is 16.7 %. The mismatch between the lattice constant *a* of Fe_3O_4 and twice of that of YSZ is 18.3 %. The mismatch between Fe_3O_4 and YSZ or ITO (17 ~ 18 %) is greatly larger than that between ITO and YSZ (1.9 %). In the pulsed-laser deposition, ITO formed single crystalline thin film, but Fe_3O_4 segregated to and formed the faceted islands on the substrate. The island looks like having a fixed shape as it grows, as shown in Fig. 3. From both electron energy loss spectroscopy and energy dispersive x-ray spectroscopy in TEM, we obtained no evidence

for coexistence of iron in the ITO matrix, and that of indium in the Fe_3O_4 NCs.

Spin Polarized Carriers and the Fe_3O_4 NCs with the [111] Axis Vertical to the Film Surface. The Fe_3O_4 NC, precipitated and grown epitaxially on the substrate, formed small angle grain boundary to the epitaxially grown ITO matrix (the upper right panel of Fig. 4). The first-principles computation was carried out to examine in detail connection in the electron density between the Fe_3O_4 (111) and In_2O_3 (002) planes. As shown in Fig. 7, the contour maps of the total electron density demonstrated smooth connection between the Fe_3O_4 (111) and In_2O_3 (002) planes. Connection between the Fe_3O_4 (111) plane and the ITO (002) plane via small angle grain boundary is anticipated to support carrier transport with lesser carrier scattering in the film.

The transport behavior in Fe_3O_4 bulk is known as a thermal activation type above T_V, and a variable range hopping $R = R_0\exp(a/T)^{1/4}$ type below T_V (22), while the ITO film, in which the Fe_3O_4 NCs exhibiting no anomaly at T_V are dispersed, demonstrated the transport character linearly fitted well with $(1/T)^{1/2}$. As shown by the ln R versus $(1/T)^{1/2}$ plots in Fig. 8, carrier transport in the film above 45 K can be fitted well by the equation of $R \propto \exp(B/T)^{1/2}$, where $B = 4\alpha/k_B N(E_F)$. Here α is the coefficient of the exponential decay of the wavefunction, k_B is the Boltzmann constant, and $N(E_F)$ is the density of states at the Fermi level. Thus, $1/\alpha$ was found to be ≈3.2 nm. Temperature dependence of resistivity fitted well with $(1/T)^{1/2}$ was reported for sputter deposited polycrystalline Fe_3O_4 films (30). The carrier transport of the film is controlled by the interface between the Fe_3O_4 NC and the ITO film, and can be explained by tunnelling conductance

mechanism (31, 32). The observed linear relation in ln R versus $T^{-1/2}$ plot indicates that a distribution of energy barriers originated in the distribution of spacing between the NCs of the film. Spin-dependent tunnelling between ferromagnetic particles resulted in tunnelling magnetoresistance of granular solids (33, 34), and tunneling magnetoresistance is proportional to the spin polarization of the tunnelling electrons (35). Observed MR of the film is based on fully spin-polarized carriers transferred from Fe_3O_4 NCs.

For another cross-sectioned specimens of the films, we reconfirmed that the [111] axis of Fe_3O_4 for each NC was vertical to the film plane. Since the [111] axis is the easy magnetization axis of the cubic Fe_3O_4 crystal, the magnetocrystalline anisotropy of Fe_3O_4 crystal brings about the spontaneous magnetization vertical to the film plane. Due to its half-metallic band structure, such Fe_3O_4 NCs can play a role of spin-aligner for the carriers of the epitaxial ITO film. As illustrated in Fig. 9, fully spin-polarized carriers of the Fe_3O_4 NCs transfer to the film, and the carriers of the film with spins parallel to the minority spins of Fe_3O_4 can pass through the NCs via E_F. Exchange interaction between carriers force the rest of carriers of ITO to align parallel to the minority spins of Fe_3O_4. A material such as the PLD-film with fully spin-polarized carriers having T_c above room temperature is anticipated to fulfill the conditions indispensable for spintronics device applications.

CONCLUSIONS

We observed that epitaxial films fabricated in oxygen partial pressures lower than 5×10^{-6} Pa by using the Fe_3O_4 nanoparticles dispersed ITO powders as a PLD target exhibited MR almost the same as that of the epitaxial grown Fe_3O_4 films. MR at 45, 75, 105, 165, and above 225 K amounted to 39, 35, 18, 5, and 3 %, respectively, in H of 1 T. R_H/R_0 increased from 0.72 to 0.97 with rise of the temperature from 45 to 225 K. In TEM, we found segregation of the Fe_3O_4 NCs from the single crystalline ITO film and formation of truncated tetrahedron of Fe_3O_4 on the YSZ substrate. Phase-separated Fe_3O_4 NCs with width of ≈40-150 nm and height of ≈10-25 nm precipitated and grew epitaxially on the substrate in the film. Both the Fe_3O_4 (111) and ITO (001) planes were parallel to the YSZ (001) plane, and the Fe_3O_4 (111) and ITO (001) planes connected smoothly at grain boundary. Such smooth connection can be simulated by the first-principles computation of the electron density distribution, support the transport character linearly fitted well with $(1/T)^{1/2}$ of the film. Since the Fe_3O_4 [111] axis for each NC was vertical to the film plane, the observed MR is based on fully spin-polarized carriers transferred from Fe_3O_4 NCs into the film. The [111] oriented Fe_3O_4 nanocrystals played a role of spin-aligner for the carriers of the epitaxial ITO film.

Acknowledgements. The authors thank for assistance of Dr. T. Ohno of Osaka University in thin film deposition, and of the staff at SAGA-Light Source in XANES experiment. They also thank Prof. T. Kawai of Osaka University and Dr. Y. Bando of National Institute for Materials Science for discussion. This work was partly supported

by the "Nanotechnology Network Project" of the Ministry of Education, Culture, Sports, Science and Technology, Japan, and the Iketani Science and Technology Foundation (0191046A).

Supporting Information Available: SQUID data of the Fe_3O_4 nanoparticles dispersed ITO powders. This material is available free of charge via the Internet at http://pubs.acs.org.

* To whom correspondence should be addressed. E-mail: kohiki@che.kyutech.ac.jp

References and notes

(1) Matsumoto,Y.; Murakami, M.; Shono, T.; Hasegawa, T.; Fukumura, T.; Kawasaki, M.; Ahmet, P.; Chikyow, T.; Koshihara, S.; Koinuma, H. *Science* **2001**, *291*, 854.

(2) Kim, D. H.; Yang, J. S.; Lee, K. W.; Bu, S. D.; Noh, T. W.; Oh, S. J.; Kim, Y. W.; Chung, J. S.; Tanaka, H.; Lee, H. Y.; Kawai, T. *Appl. Phys. Lett*. **2002**, *81*, 2421.

(3) Ueda, K.; Tabata, H.; Kawai, T. *Appl. Phys. Lett*. **2001**, *79*, 988.

(4) Kim, J. H.; Kim, H.; Ihm, Y. E.; Choo, W. K. *J. Appl. Phys*. **2002**, *92*, 6066.

(5) Sharma, P.; Gupta, A.; Rao, K. V.; Owens, F. J.; Sharma, R.; Ahuja, R.; Guillen, J. M. O.; Johansson, B.; Gehring, G. A. *Nat. Mater*. **2003**, *2*, 673.

(6) Ogale, S. B.; Choudhary, R. J.; Buban, J. P.; Lofland, S. E.; Shinde, S. R.; Kale, S. N.; Kulkarni, V. N.; Higgins, J.; Lanci, C.; Simpson, J. R.; Browning, N. D.; Das Sarma, S.; Drew, H. D.; Greene, R. L.; Venkatesan, T. *Phys. Rev. Lett*. **2003**, *91*, 077205.

(7) Coey, J. M. D.; Douvalis, A. P.; Fitzgerald, C. B.; Venkatesan, M. *Appl. Phys. Lett*. **2004**, *84*, 1332.

(8) Philip, J.; Theodoropoulou, N.; Berera, G.; Moodera, J. S.; Satpati, B. *Appl. Phys. Lett*. **2004**, *85*, 777.

(9) Hong, N. H.; Sakai, J.; Huong, N. T.; Poirot, N.; Ruyter, A. *Phys. Rev*. B **2005**, *72*, 045336.

(10) Yoo, Y. K.; Xue, Q.; Lee, H. C.; Cheng, S.; Xiang, X. D.; Dionne, G. F.; Xu, S.; He, J.; Chu, Y. S.; Preite, S. D.; Lofland, S. E.; Takeuchi, I. *Appl. Phys. Lett*. **2005**, *86*, 042506.

(11) He, J.; Xu, S.; Yoo, Y. K.; Xue, Q.; Lee, H. C.; Cheng, S.; Xiang, X. D.; Dionne, G. F.; Takeuchi, I. *Appl. Phys. Lett*. **2005**, *86*, 052503.

(12) Hong, N. H.; Sakai, J.; Huong, N. T.; Brize, V. *Appl. Phys. Lett*. **2005**, *87*, 102505.

(13) Kim, H. S.; Ji, S. H.; Kim, H.; Hong, S. K.; Kim, D.; Ihm, Y. E.; Choo, W. K. *Solid State Commun*. **2006**, *137*, 41.

(14) Philip, J.; Punnoose, A.; Kim, B. I.; Reddy, K. M.; Layne, S.; Holmes, J. O.; Satpati, B.; Leclair, P. R.; Santos, T. S.; Moodera, J. S. *Nat. Mater*. **2006**, *5*, 298.

(15) Hong, N. H.; Sakai, J.; Huong, N. T.; Brize, V. *J. Mag. Mag. Mater*. **2006**, *302*, 228.

(16) Peleckis, G.; Wang, X. L.; Dou, S. X. *Appl. Phys. Lett*. **2006**, *88*, 132507.

(17) Peleckis, G.; Wang, X. L.; Dou, S. X. *Appl. Phys. Lett*. **2006**, *89*, 022501.

(18) Ohno, T.; Kawahara, T.; Tanaka, H.; Kawai, T.; Oku, M.; Okada, K.; Kohiki, S. *Jpn. J. Appl. Phys*. **2006**, *45*, L957.

(19) Shinde, S. R.; Ogale, S. B.; Higgins, J. S.; Zheng, H.; Millis, A. J.; Kulkarni, V. N.; Ramesh, R.; Greene, R. L.; Venkatesan, T. *Phys. Rev. Lett*. **2004**, *92*, 166601.

(20) Okada, K.; Kohiki, S.; Nishi, S.; Shimooka, H.; Deguchi, H.; Mitome, M.; Bando, Y.; Shishido, T. *Jpn. J. Appl. Phys*. **2007**, *46*, L823.

(21) P.; Blaha, Schwartz, K.; H. Madsen, G. K.; Kvasnicka, D.; Luitz, J. *WIEN2k, An Augmented Plane Wave + Local Orbitals Program for Calculating Crystal Properties*; Tech. Universitat Wien, Vienna, Austria: 2001.

(22) Ogale, S. B.; Ghosh, K.; Sharma, R. P.; Greene, R. L.; Ramesh, R.; Venkatesan, T. *Phys. Rev*. B **1998**, *57*, 7823.

(23) Goya, G. F.; Berquó, T. S.; Fonseca, F. C.; Morales, M. P.; *J. Appl. Phys*. **2003**, *94*, 3520.

(24) Eerenstein, W.; Palstra, T. T. M.; Hibma, T.; Celotto, S. *Phys. Rev*. B **2002**, *66*, 20110(R).

(25) Sigmoidal behavior of magnetization *M* was observed in the field $H > \pm 2000$ Oe at 10 K. The order of *M* of the sample grown below the oxygen partial pressure of 5×10^{-6} Pa was 10^{-4} emu, which is larger by two orders of the magnitude than that for the films grown at the oxygen partial pressures of 1×10^{-1} Pa - 1×10^{-3} Pa (Ohno, T.; Kawahara, T.; Murasugi, M.; Tanaka, H.; Kawai, T.; Kohiki, S. *J. Magn. Magn. Mater.* **2007,** *310*, e717).

(26) Change in the Hall resistance below the magnetic field of ±1000 Oe amounted to 0.3 Ω/Oe, which is larger than that (0.02 Ω/Oe) in the field ranging from ±1000 to ±10000 Oe. Since such changes are an indication of spin polarization of the film, x-ray magnetic circular dichroism measurement at the Fe $L_{2,3}$ edges using synchrotron radiation is indispensable for assertion.

(27) Subías, G.; García, J.; Blasco, J. *Phys. Rev*. B **2005**, *71*, 155103.

(28) The upper (111) plane of the Fe_3O_4 NC is widely spreading and contacting to ITO. If wider contact to ITO lowers more the surface energy for the NC, the NC surrounded by the (111) planes becomes more stable, and then the truncated octahedron is the most promising for the shape of Fe_3O_4 NC.

(29) Tersoff J.; LeGoues, F. K. *Phys. Rev. Lett*. **1994**, *72*, 3570.

(30) Liu, H.; Jiang, E. Y.; Bai, H. L.; Zheng, R. K.; Wei, H. L.; Zhang, X. X.; *Appl. Phys. Lett*. **2003**, *83*, 3531.

(31) Sheng, P. *Phys. Rev*. B **1980**, *21*, 2180.

(32) Sheng, P. *Philos. Mag*. B **1992**, *65*, 357.

(33) Mitani, S.; Takahashi, S.; Takanashi, K.; Yakushiji, K.; Maekawa, S.; Fujimori, H. *Phys. Rev. Lett*. **1998**, *81*, 2799.

(34) Spin-dependent tunnelling between the Fe_3O_4 NCs is anticipated to cause significant tunnelling magnetoresistance for the sample demonstrating semiconducting behavior. The first-principle computation on the Fe_3O_4 (110) / In_2O_3 (010) interface was performed to obtain a better insight into the band structure in the vicinity of the atomically sharp Fe_3O_4 and ITO heterointerface. The interface was simulated by building up supercells consisting of the Fe_3O_4 (110) layers on top of the In_2O_3 (010) layers. The density of states (DOS) of Fe_3O_4 (110) was metallic and that of In_2O_3 (010) was semiconducting. At the In_2O_3 side, a large *p*-type DOS crossing E_F appeared in the layer positioned by 0.6 nm apart from the interface. Electrons doped to In_2O_3 occupy the empty states from 1-2 eV in the layer locating next to the Fe_3O_4 surface. Therefore, nonmetallic carrier transport is rather reasonable in the vicinity of the Fe_3O_4 and ITO heterointerface. We will report on the computation in detail elsewhere.

(35) Inoue J.; Maekawa, S. *Phys. Rev.* B **1996**, *53*, R11927.

Figure captions

Figure 1. (Color online) XRD pattern in the vicinity of the YSZ (200) and ITO (400) reflections (upper panel). The peaks from magnetite (311), hematite (110), and maghemite (311) planes appear at 2θ = 35.453^{o} (JCPDS 19-0629), 35.642^{o} (JCPDS 33-0664), and 35.661^{o} (JCPDS 39-1346), respectively, in XRD with Cu $K\alpha$ x-rays. The intensity of the figure is Log and that of the inset is normal. HRTEM image around interface between the film and the substrate (lower panel).

Figure 2. R_H (open circle) and R_0 (closed circle) of the film (left scale) with H = 1 T applied in the film plane. *FC* (open circle) and *ZFC* (filled circle) *M-T* data at H = 100 Oe (right scale). Inset: temperature dependence of R_H/R_0.

Figure 3. TEM images (upper panels) and Fe-maps (lower panels) for smaller NC (left) and larger NC (right). The Fe-maps obtained from the Fe L_3 electron energy loss signal represent distribution of iron atoms in the film.

Figure 4. (Color online) HRTEM image (upper panel), SAED pattern (middle panel) and indices corresponding to the SAED pattern (lower panel) for the NC epitaxially grown on the substrate (left), and those for the NC and the film epitaxially grown on the substrate (right). Electron beam incidence was [1-10] on Fe_3O_4 and [100] on YSZ (left), and that was [11-2] on Fe_3O_4 and [100] on both ITO and YSZ (right). The mark × in the lower left panel corresponds to {112} reflections. Epitaxial relations are Fe_3O_4 (111) // YSZ (001), Fe_3O_4 [110] // YSZ [100], Fe_3O_4 [1-1-2] // YSZ [010], ITO (001) // YSZ (001), ITO [100] // YSZ [100], and ITO [010] // YSZ [010].

Figure 5. XANES spectrum at the Fe *K* edge of the film.

Figure 6. Illustration of the Fe_3O_4 NC on the YSZ substrate in the ITO film.

Figure 7. (Color online) Contour maps of the total electron density of the Fe_3O_4 (111) and In_2O_3 (002) planes. The [11-2] and [220] axes of Fe_3O_4 are parallel to the [200] and [0-20] axes of In_2O_3, respectively.

Figure 8. Temperature dependence of resistance of the film as a function of $(1/T)^{1/2}$.

Figure 9. Schematic representation of the ITO film containing the [111] oriented Fe_3O_4 NCs. Only the density of states of Fe^{2+} ions in octahedral sites was depicted for representing the half-metallicity of Fe_3O_4. Charge carriers of Fe_3O_4 are fully spin-polarized $(t_{2g\downarrow})^1$ at E_F. Even in a field *F*, only carriers of ITO with spins parallel to the minority spins of Fe_3O_4 pass through the NC. The Fe_3O_4 NCs play a role of spin-aligner for the carriers itinerating around the conduction band of the ITO film.

Fig.1 K.O et al.

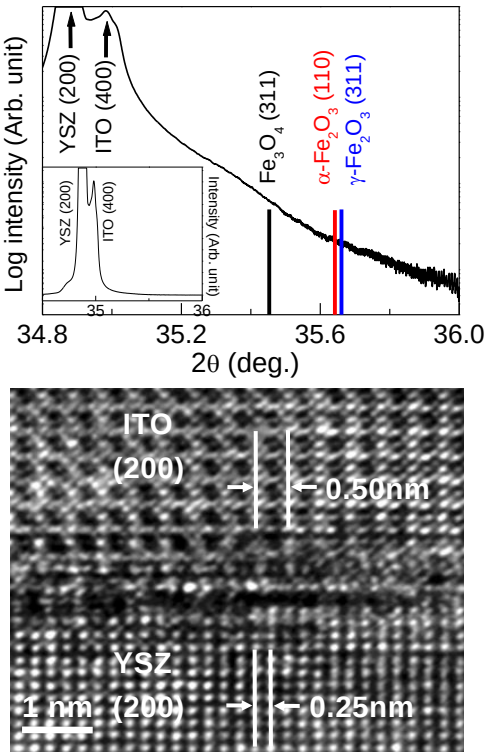
Log intensity (Arb. unit)
YSZ (200)
ITO (400)
Fe3O4 (311)
α-Fe2O3 (110)
γ-Fe2O3 (311)
Intensity (Arb. unit)
35
36
34.8
35.2
35.6
36.0
2θ (deg.)
ITO
(200)
0.50nm
YSZ
1 nm
(200)
0.25nm

Fig.2 K.O et al.

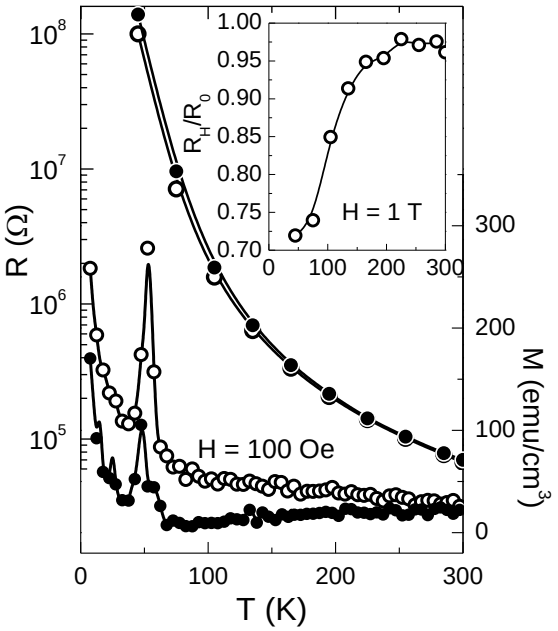

Fig.3 K.O et al.

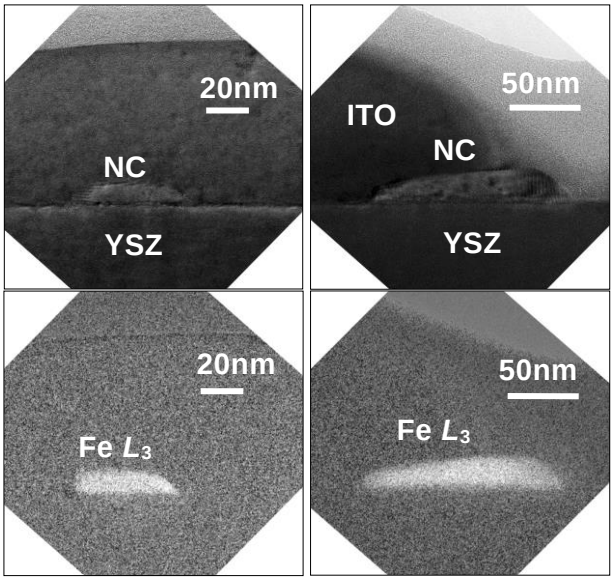

Fig.4 K.O et al.

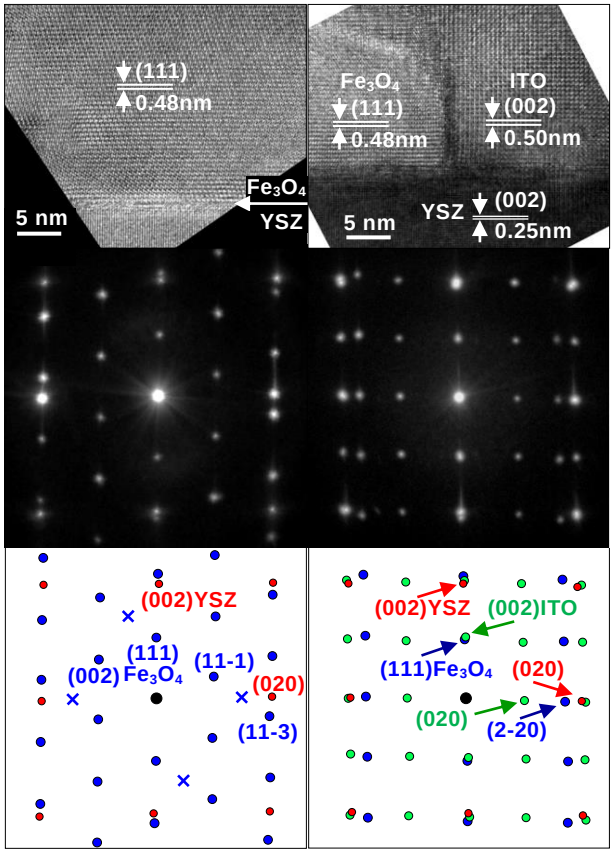
(111)
0.48nm
5 nm
Fe3O4
YSZ
Fe3O4
(111)
0.48nm
ITO
(002)
0.50nm
5 nm
YSZ
(002)
0.25nm
(002)YSZ
(111)
(11-1)
(002)Fe3O4
(020)
(11-3)
(002)YSZ
(002)ITO
(111)Fe3O4
(020)
(020)
(2-20)

Fig.5 K.O et al.

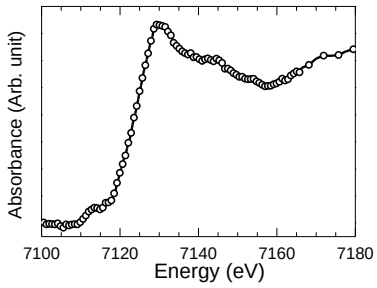

Fig.6 K.O et al.

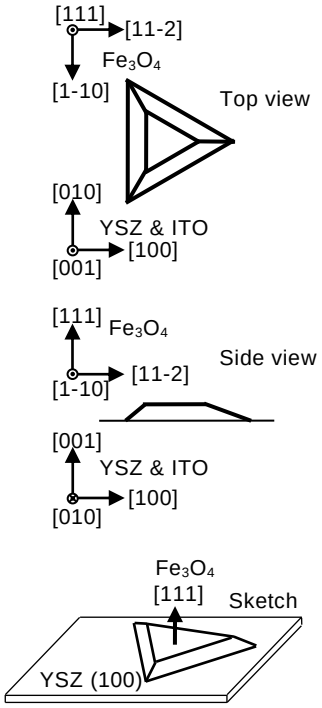
[111]
[11-2]
Fe3O4
[1-10]
Top view
[010]
YSZ & ITO
[100]
[001]
[111]
Fe3O4
Side view
[11-2]
[1-10]
[001]
YSZ & ITO
[100]
[010]
Fe3O4
[111]
Sketch
YSZ (100)

Fig.7 K.O et al.

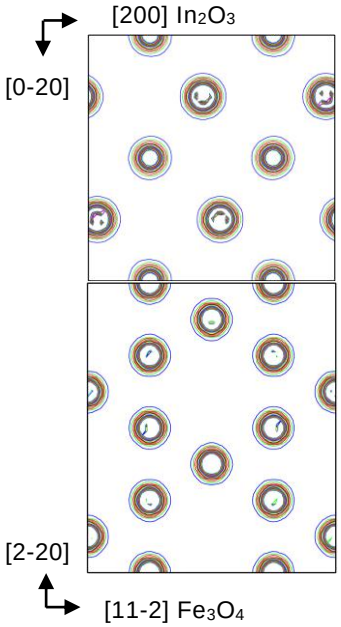

Fig.8 K.O et al.

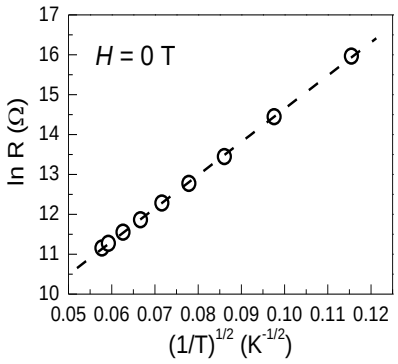
H = 0 T
ln R (Ω)
(1/T)^1/2 (K^-1/2)
17
16
15
14
13
12
11
10
0.05 0.06 0.07 0.08 0.09 0.10 0.11 0.12

Fig.9 K.O et al.

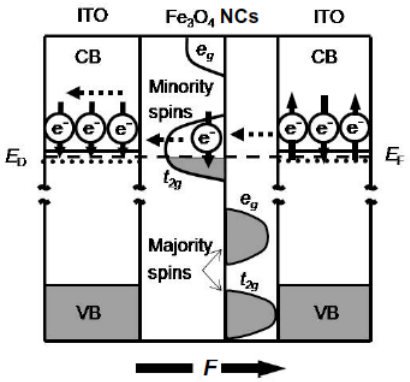
ITO
Fe3O4 NCs
ITO
CB
CB
eg
Minority
spins
e-
e-
e-
e-
e-
e-
e-
ED
EF
t2g
eg
Majority
spins
t2g
VB
VB
F

TOC Figure K.O